Compositional modelling and crushing behaviour of MSWI bottom ash material classes

P.M.F. van de Wouw *, E. Loginova, M.V.A. Florea, H.J.H. Brouwers

Department of the Built Environment, Unit Building Physics and Services, Eindhoven University of Technology, P.O. Box 513, 5600 MB Eindhoven, the Netherlands

ABSTRACT

At present, in Europe, 18 million tonnes of MSWI Bottom Ash (BA) is annually stockpiled or used in low-grade applications (e.g. in road bases). Therefore, alternative applications, such as aggregate or as a cement component in concrete, are stimulated. Physical and chemical characteristics remaining after treatment, however, prevent its extensive application in building materials. Hence, knowledge is needed on the distinct properties of the material classes making up a heterogeneous BA, enabling the assessment of its characteristics and the resulting applicability. Furthermore, a user-friendly composition assessment procedure is necessary to evaluate the output of physical treatment processes. Crushing is a commonly applied treatment and its effect on the material classes comprising BA is still unknown. In this paper, the latter are identified and classified into slag, magnetic slag, glass, refractory, metals, and unburned material classes. The individual characteristics of each material class are identified and a suitable tracer for tracking these classes in heterogeneous samples is defined. Furthermore, a fast method to quantify the distribution of material classes based just on the oxide composition is developed and applied to approximate the changes in the configuration of BA through crushing. It is concluded that, although the jaw crushing of BA results in a more homogeneous distribution, beneficiation of material classes occurs and selective crushing is possible in order to improve the quality of the BA and therefore its subsequent application.

1. Introduction

The incineration of municipal solid waste (MSWI) is the preferred alternative to landfilling since a significant mass and volume reduction is achieved, by approximately 70% and 90%, respectively (Chimenos et al., 1999), and electric power and hot water are produced. Even though the mass and volume are reduced significantly, in Europe, approximately 18 million tonnes of bottom ash (BA), the main incineration residue, is produced annually (CEWEP, 2015, 2014). The BA is being stockpiled, has a limited application as road base material (Allegrini et al., 2015; Dabo et al., 2009; Florea and Brouwers, 2013; Grosso et al., 2011; Pecqueur et al., 2001; CEWEP, 2015), and in the Netherlands, an application as aggregate in concrete is becoming more accepted for some specifically treated BA size fractions (Keulen et al., 2016, 2012). Furthermore, the use as raw material for the production of cements or pozzolans is promising (Al-Rawas et al., 2005; Arickx et al., 2007; Dhir et al., 2017; Ferraris et al., 2009; Hyks et al., 2011; Juric et al., 2006; Li et al., 2012; Lin and Lin, 2006; Pan et al., 2008; Qiao

et al., 2008b; Tang et al., 2016b). In general, alternative applications are stimulated through stricter legislation, landfill taxes, and landfilling bans (Al-Rawas et al., 2005; CEWEP, 2017; Su et al., 2013; Yang et al., 2012).

Despite its heterogeneity, BA has comparable properties to those of virgin resources used in the production of building materials, so it potentially can be altered to fit this application (Al-Rawas et al., 2005; Bertolini et al., 2004; del Valle-Zermeño et al., 2013; Saikia et al., 2008). In the case that BA is applied in concrete (globally, $33 \cdot 10^9$ tonnes of concrete, accounting for $27 \cdot 10^9$ tonnes of aggregates per year (Mehta and Monteiro, 2014)), not only the landfilling of this by-product, but also the mining of raw materials and the concrete CO_2 production footprint can be reduced (Al-Rawas et al., 2005; Chimenos et al., 1999; del Valle-Zermeño et al., 2013; Wiles, 1996), making this a more sustainable approach. When replacing traditional concrete constituents with BA, the environmental legislation is directive since these industrial by-products might contain leachable heavy metals and salts (Su et al., 2013; Yang et al., 2012). Several treatments, e.g. physical separation (Grosso et al., 2011), solidification/stabilization (Chandler et al., 1997; Mangialardi et al., 1999; Quina et al., 2008), carbonation (Arickx et al., 2006; Meima et al., 2002), weathering

* Corresponding author.
E-mail address: p.m.f.v.d.wouw@tue.nl (P.M.F. van de Wouw).

(Grosso et al., 2011; Meima and Comans, 1999), washing (Cossu et al., 2012; Grosso et al., 2011; Lin et al., 2011; Steketee et al., 1997), and heat treatment (Arickx et al., 2007; Hyks et al., 2011; Qiao et al., 2008b; Tang et al., 2016b) have been proven to be effective in lowering the environmental impact of the BA to meet these requirements. Furthermore, the use of binders in concrete enables the immobilization of a part of the leachable elements present in BA (Eijk, 2001; Florea et al., 2016). The replacement of coarse aggregates with BA was investigated in multiple studies and in some conditions successfully applied (Cioffi et al., 2011; Juric et al., 2006; Keulen et al., 2016; Li et al., 2012; Müller and Rübner, 2006a; Quenee et al., 2000; Siddique, 2010; Sorlini et al., 2011; Tang et al., 2016a).

In practice, there are, however, several problems related to specific materials found in BA which prevent an extensive application as aggregate, mainly due to the following physical and chemical characteristics:

- the Al^0 content can cause early age expansion through hydrogen formation (Cioffi et al., 2011; Müller and Rübner, 2006a; Pecqueur et al., 2001);
- the glass content induce late expansion caused by alkali-silica reaction (Cheng, 2012; Müller and Rübner, 2006a);
- the quenching product of melt products provide a substantial specific surface area and active pores (Inkaew et al., 2015; Tang et al., 2015), increasing the overall water demand, are believed to be the main host for chemical reactions during weathering, and plays a key role in the accumulation and distribution of i.a. chlorides (Alam et al., 2019a, 2017; Inkaew et al., 2016, 2015; Yang et al., 2014) of which the leaching is restricted by legislation (Dutch Soil Quality Decree, 2007).

Hence, with the implementation of heterogeneous coarse BA in concrete, the final properties can be affected by varying ratios of its composing material classes (henceforth called "classes") which are classified in Section 3.1.1. As a result, current specific treatments are aimed at minimising these variations. In practice, however, the application of more homogeneous industrial by-products (e.g. recycled concrete aggregates, bricks, and glass) in concrete is more widely accepted than that of the heterogeneous BA (Florea et al., 2014; Florea and Brouwers, 2013; Hansen, 1992; McNeil and Thomas, 2013; Pacheco Torgal, 2013; Silva et al., 2014; Spiesz et al., 2016). Hence, homogeneous materials (so-called "monostreams") created out of BA are likely to be more easily applicable and/or accepted. By selectively crushing distinct BA classes, the goal is to create more homogeneous streams and to remove contaminants which are concentrated in the quenching products (Alam et al., 2019a; Inkaew et al., 2016, 2015; Tang et al., 2016b; Yang et al., 2014).

The crushing of BA is a common practice, whereby different types of impact and jaw crushers are applied (Holm and Simon, 2017). In general crushing is used to achieve various degrees of size reduction (Meima and Comans, 1997; Qiao et al., 2008a, 2008b) and to improve further treatment steps, e.g. the extraction of valuable metals (Biganzoli et al., 2013; Manders, 2009; Vries et al., 2009) by liberating the bonded and agglomerated materials which occur after weathering (Holm and Simon, 2017). Additionally, the crushing of BA is suggested to improve the technical quality of the particles for road base applications (Vegas et al., 2008). The actual effects of crushing on the classes of various BA size fractions were never reported in the literature, to the best of the authors' knowledge.

The crushing of BA could have potentially negative side-effects. When aged and weathered grains are broken, new surface area is created, and fresh surfaces and embedded metals are exposed (Dabo et al., 2009; Meima and Comans, 1997). Additionally, Holm

and Simon classify the crushing of BA to be a "process with high energy consumption and a high degree of wearout" (Holm and Simon, 2017). This approach is, however, still worthwhile because of the increased efficiency of further treatments, the improvement of the technical quality and of the recovery of metals (Biganzoli et al., 2013; Manders, 2009; Vries et al., 2009).

In this research, a coarse BA size fraction (2.0–31.5 mm) is studied with the aim of applying crushing for the beneficiation of classes into specific size fractions (hereinafter called "fractions"). The goal is to create less heterogeneity, to concentrate the contamination present in melt products in the fines, and to create better applicability for the clean fraction. To this end, the BA is not considered as a single heterogeneous material, but as a mix of distinct material classes, making up the complete material.

This paper provides the identification and classification of materials comprising BA into classes of slag, magnetic slag, glass, refractory, metals, and unburned organics. Additionally, the individual characteristics of each identified class are determined. A practical tracer for tracking classes in heterogeneous samples is identified and a fast method to quantify the distribution of classes is proposed. Finally, this model is applied to approximate the changing composition through crushing.

2. Materials and methods

The MSWI BA considered in this study was obtained from a municipal solid waste-to-energy incinerator located in the Netherlands. The investigated 2.0–31.5 mm granulate fraction is one of several size fractions produced in the prior treatment process, schematically shown in Fig. 1. Regardless of different production processes, it has been shown that the physical and chemical properties of bottom ashes from different waste-to-energy plants are very similar and stable over time (Tang et al., 2015).

Fig. 2 displays the sample preparation, treatment, and testing procedure followed in this study. During the sample stage (Fig. 2, stage 1), approximately 100 kg of the 2.0–31.5 mm MSWI BA fraction was sampled from ten different sampling points from a stockpile. These were combined and mixed to create a representative material. Consecutively, it was oven-dried to a constant mass at 105 °C, split into 32 samples by means of riffle splitter, and recombined to 6 samples in accordance with (EN 932-1, 1996) and (EN 932-2, 1999), ensuring a homogeneous mixture.

The specific density of materials was measured using a He pycnometer (Micrometrics AccuPyc 1340) (Fig. 2, B).

In the separation stage (Fig. 2, stage 2a), 3 out of 6 non-crushed samples of BA (hereinafter called initial BA) were drily sieved according to (EN 933-1, 2012; EN 933-2, 1995) with the addition of sieves with the following mesh sizes: 22.4 mm, 11.2 mm, 5.6 mm, 2.8 mm, 1.4 mm, 710 μm, 355 μm, 180 μm, and 91 μm. Hence, the PSD was determined (Fig. 2, A) and the material split into 20 corresponding size fractions. For fine particles present (adhered to the coarse particles) passing the 63 μm sieve, the PSD was determined by laser diffraction spectroscopy (Malvern Instruments, Mastersizer 2000) in water. The size fractions larger than 4 mm were hand-separated based on their visual appearance (Section 3.1.1). Additionally, ferrous metal-containing particles were sequentially extracted three times by placing several particles onto a permanent magnet (110.6 × 89 × 19.5 mm, NdFeB, 860–995 kA/m) and slowly rotating it upside down, emulating a magnetic drum separator and resulting in the extraction of magnetic materials. Successively (Fig. 2, C), the aggregate crushing values (ACV) were determined in correlation with the British Standard crushing value test, Appendix A (BS 812: Part 110, 1990).

During the crushing stage (Fig. 2, stage 2b), the remaining 3 samples of BA were crushed by passing the initial BA a single time
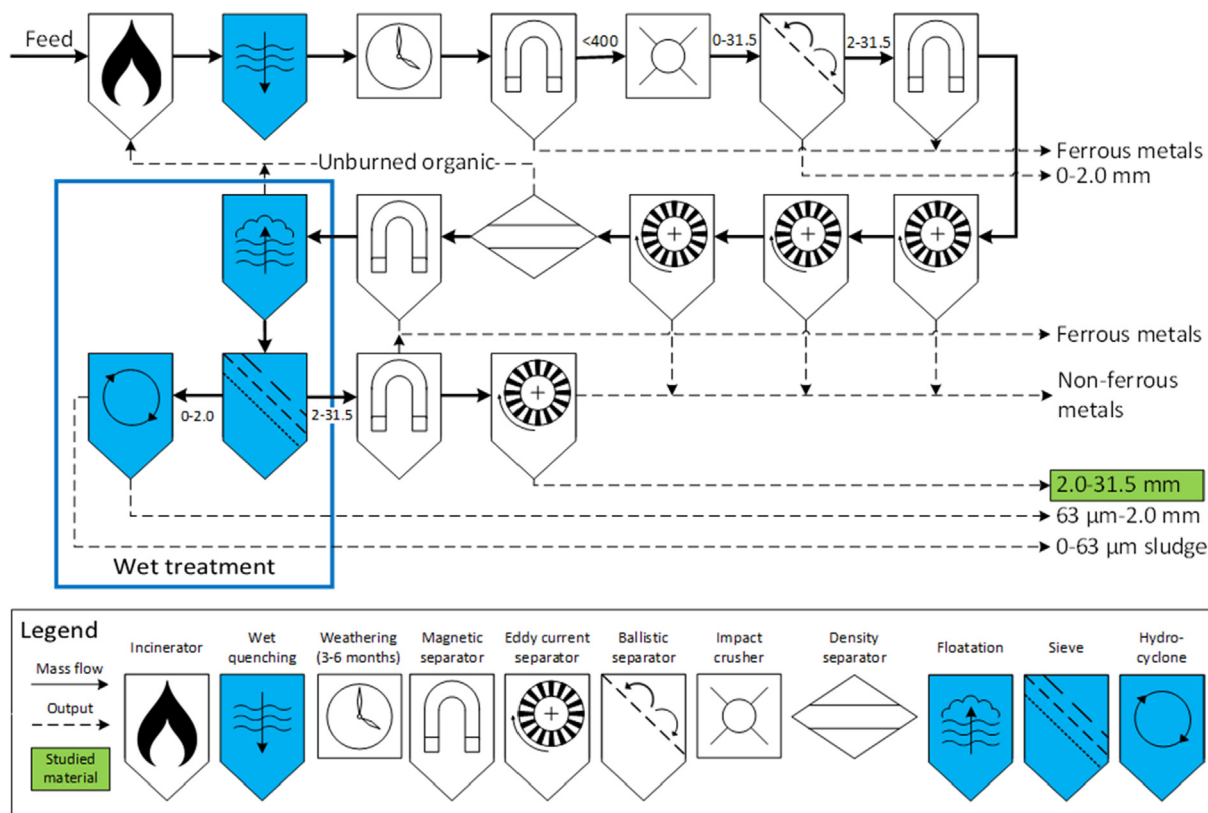
Fig. 1. The preceding BA treatment process scheme.

through a lab-scale jaw crusher (Retsch BB-2) fitted with waved manganese steel jaws set to a closed side setting (CSS) of 8 mm. The obtained material (hereinafter called crushed BA) was sieved in the same way as the initial BA and their PSD determined (Fig. 2, A).

After both the crushing and the separation stages, all fractions produced underwent identical analysis preparation (Fig. 2, stage 3). The fractions larger than 4 mm were crushed using the jaw crusher mentioned above. Subsequently, as described in (Tang et al., 2016b), all fractions were slowly milled to powder in a planetary ball mill (Fritsch PULVERISETTE 5) fitted with zirconium oxide grinding bowls and 20 mm mill balls for a total of 100 min with a 5-minute break every 10 min at 200 rpm. Successively, all powders produced were sieved at below 125 μm. Hence, metals were predominantly extracted in this process since they were not milled to a powder and remain present as either larger or flattened particles after the milling process. The extracted material >125 μm accounts for less than 1% of the total and is therefore considered negligible.

All thermal analyses of all samples, both thermogravimetric analyses (TG) and differential scanning calorimetry (DSC) were performed in an inert atmosphere (N_2, 20 mL/min) using a Netzsch STA 449 F1 Jupiter (Fig. 2, D). TG analysis was used to determine the loss on ignition (LOI) of the materials by measuring the mass loss of samples at 950 °C to a constant mass. DSC analysis was simultaneously performed to determine the quartz content of the various classes and size fractions using the crystalline phase change from α-quartz to β-quartz (Shui et al., 2008). The thermal analysis was performed in Pt crucibles up to a maximum temperature of 640 °C. The peak area on the DSC curve of the fourth heating step was analysed and correlated to measurements of samples containing a known amount of α-quartz, whereby the quartz con-

tent of the measured samples was quantified (Florea, 2014; Florea and Brouwers, 2013, 2012).

The mineralogical composition of the BA classes was determined by X-ray diffraction (XRD) (Fig. 2, E) using a Bruker D2 PHASER (Co tube, 1.79026 [Å], step size 0.02°2Θ, range 5–60°2Θ) with a LYNXEYE 1-D detector and fixed divergence slits. The XRD measurements were performed on pre-dried powdered samples. Phase identification was done using X'Pert HighScore Plus 2.2 and the PDF-2 database.

Prior to the preparation of the fused beads, the materials were oxidised in air at 950 °C according to (EN 196-2, 2013), in turn reducing the influence of organics present. The bulk concentration of elements in the materials (computed as oxide forms) was determined by energy-dispersive X-ray fluorescence (EDXRF) using a PANalytical Epsilon 3 instrument (a 9 W/50 kV Rh X-ray tube, a silicon drift detector) equipped with Omnian software 1.0.E (PANalytical) (Fig. 2, F). The samples for EDXRF were 40-mm fused beads prepared from pre-dried powdered samples, 0.95 g, with a 67.00% $Li_2B_4O_7$ – 33.00% $LiBO_2$ flux, 9.50 g; and 0.32 mL of a 4 M LiBr solution as a non-wetting agent using a LeNeo fluxer (Claisse) at 1065 °C.

3. Results and discussion

3.1. Classes: identification and characterisation

3.1.1. Identified classes

The BA comprises different materials for which the following classes are proposed in the literature: minerals (e.g. quartz, calcite, feldspars, lime), ceramics, glass, ferrous and non-ferrous metals, and unburned organic matter (Chimenos et al., 1999). Within the
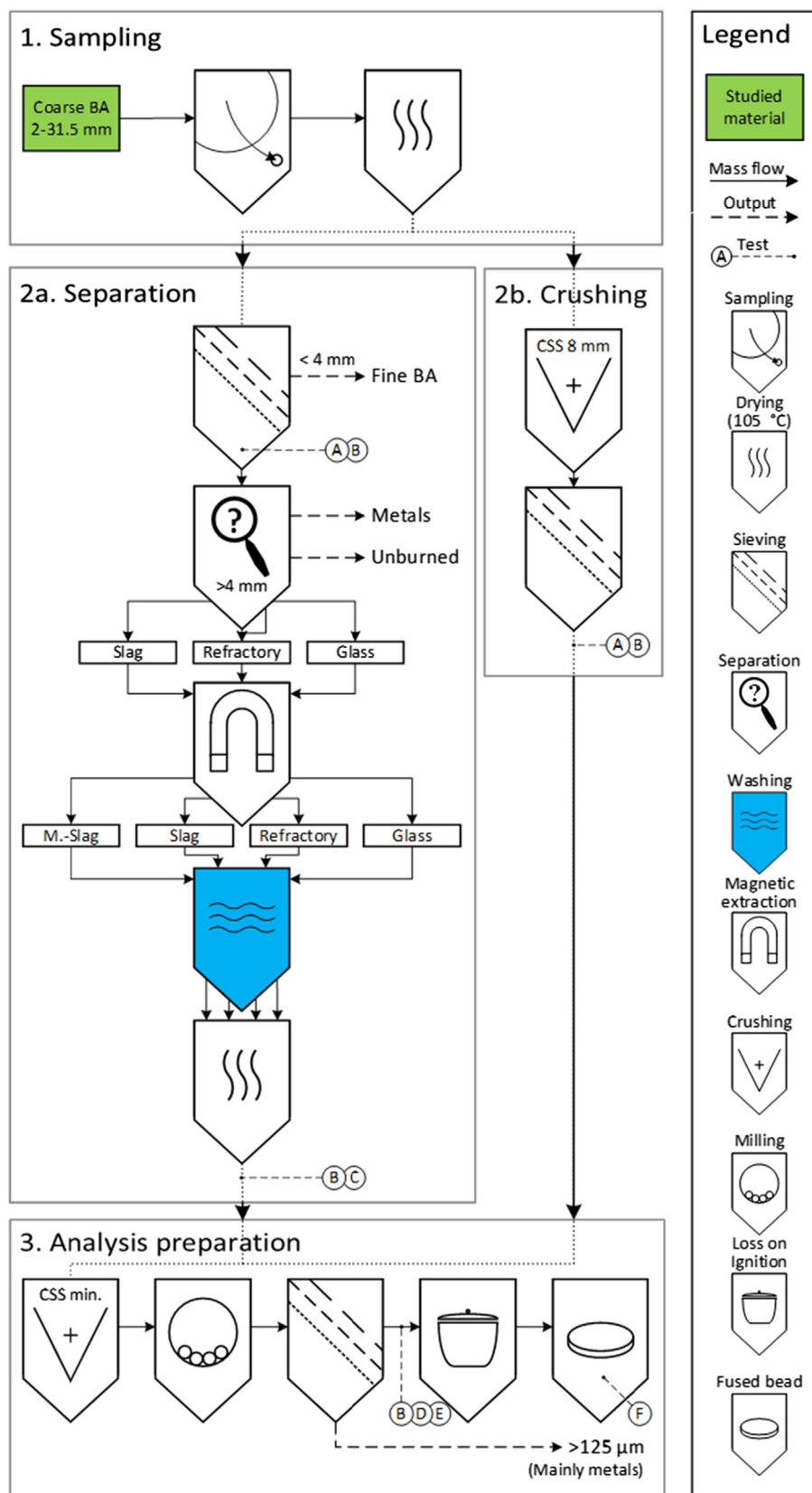
Fig. 2. Sample preparation procedure with measurements for: a. Particle size distribution, b. Specific density, c. Aggregate crushing value, d. Thermogravimetric analyses and differential scanning calorimetry, e. X-ray diffraction, f. X-ray fluorescence.

Fig. 3. Hand-separated material classes: a. Slag, b. Metals, c. Glass, d. Refractory, e. Unburned of size fractions 4.0–31.5 mm.

Fig. 4. The mean configuration of classes in 4–31.5 mm MSWI BA fractions.

BA two main products can be identified: melt products and refractory materials (Inkaew et al., 2016). Additionally, a small quantity of unburned materials is present. Separation of the BA is performed based on their visual appearance (Fig. 3a–e) according to the following classification:

The slag class (Fig. 3a) comprises melt products which are formed during incineration and is characterised by the presence of porous quench products (Inkaew et al., 2015; Wei et al., 2011a; Yang et al., 2014). The refractory materials are remaining from the municipal solid waste and maintain their original characteristics after the incineration (Eusden et al., 1999; Saffarzadeh et al., 2006). This group consists of ceramics, metals, and other constituents. In this study, the refractory group is subdivided into metals, glass, and residual refractory materials. Since metals (Fig. 3b) are unaffected by incineration, they can partially be easily recognised based on their shape (e.g. screws, wires, coins, platy chunks, etc.). Glass particles (Fig. 3c) are generally found to be clean and translucent and are, therefore, easily recognisable as well. The residual refractory materials (Fig. 3d) is a group of unaltered materials composed of ceramics, rock, and mineral fragments (hereinafter called refractory). Unburned organic matter (unburned) (Fig. 3e) consists of combustible materials which passed through the incinerator (semi)unaffected. This class consists of e.g. paper, organics, and different types of plastic.

On account of sufficient recognisability, 3 independent sets of 6 fractions larger than 4 mm were hand-separated into the abovementioned 6 classes. When multiple classes were present in a single particle (e.g. slag molten on a glass particle, circled in Fig. 3c) this particle was classified by the predominant class, generally >80%.

3.1.2. Magnetic separation

Despite prior treatments, both clean metallic particles and classes containing embedded metals could still be identified. As a result of ferrous material included in melt products, a large amount of exclusively slag particles could be extracted by a magnet. Hereinafter, this class is referred to as magnetic slag (M-slag). The non-magnetic residual share is referred to as slag. On average, 70% of the mass of the total slag class contains enough ferrous metals to be extracted by use of a strong magnet. Overall, this accounts for 32.5% by mass of the total 4–31.5 mm BA. The extracted M-slag can either be crushed to liberate and extract present metals, or used in a specific application e.g. as an alternative adsorbent in the desulfurization of biogas (Fontseré Obis et al., 2017).

Fig. 4 shows the plot of the distribution of the classes within the various size fractions. With only a minor deviation in the 22.4–31.5 mm size fraction, a correlation between the content of M-slag and slag can be seen. From this, it also becomes clear that
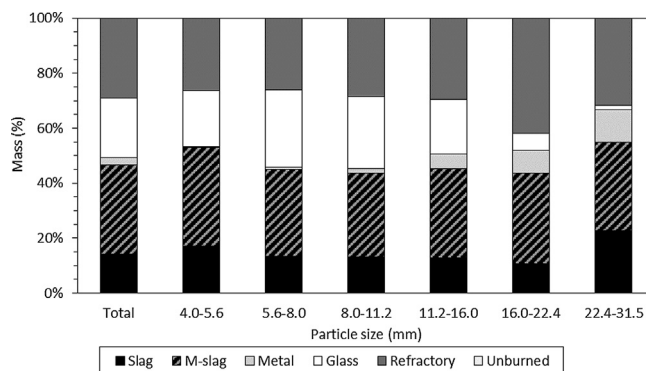
the M-slag and refractory together make up the majority of the 4–31.5 mm BA, thereby greatly determining the overall PSD. In general, the fractions of the M-slag, slag, and refractory classes show a good relation to the average PSD of the overall BA. Conversely, metals are found to be less present in the smaller size fractions, whereas glass shows an opposite trend, having only a few larger particles.

For the initial 4–31.5 mm BA, with increasing particle size, an increasing metal content can be perceived ranging from 0.4% in the 4.0–5.6 mm fraction to 11.7% in the 22.4–31.5 mm size fraction, consistent with the findings of del Valle-Zermeño et al. (2017). The metal content found within the investigated BA is still relatively high, considering the numerous prior metal extraction steps. The increase in metal content with increasing particle size can be related to separation treatments (e.g. ballistic separation) which could be influenced by the variation in density of the various classes. Additionally, their ductility makes them less susceptible to size reduction due to the low rate of stress during handling and crushing, resulting in a size close to the starting size (Fayed and Otten, 1997). A different effect is observed in the glass content over the size fractions. Here, with an increase in particle size, initially, a slight increase in the glass content is witnessed from 20.4% to 28.1% for respectively the 4.0–5.6 mm and 5.6–8 mm size fraction, after which its quantity strongly decreases to 1.7% in the 22.4–31.5 mm size fraction, in accordance with literature (del Valle-Zermeño et al., 2017). This can be explained by the brittle and highly flaky nature of the glass in the larger particle sizes. Through processing, handling, and pre-crushing, the glass is likely to fracture into smaller pieces down to the point where the particles are more spherical than flaky. A similar, yet not so obvious phenomenon, can be seen in the refractory class. In line with the literature (del Valle-Zermeño et al., 2017), the content is nearly constant at 28% by mass on average, except for the 16–22.4 mm size fraction where this accounts for 42%. Typically, this class has a flaky and brittle nature as well, however, the particles are thicker, making it more resilient to fracturing under the same conditions. In addition, an overall slight decrease in the slag content can be seen, up to the 22.4–31.5 mm size fraction where an increase in content is observed. Except for the latter, the trend agrees with literature (del Valle-Zermeño et al., 2017). In contrast to the glass and the refractory classes, which are platy and angular shaped due to their pre-incinerated shape and subsequent fracturing, this material is found to approximate a shape closer to spherical throughout all size fractions. This could be related to its brittle and porous nature, through which small angular corners are easily broken off, releasing the stresses introduced by the various treatments and general handling. Consequently, this results in a lower amount of particles splitting into smaller size fractions and resulting in a less angular material in the larger fractions. The unburned matter is

predominantly concentrated in the 5.6–8.0 mm size range, as per literature (del Valle-Zermeño et al., 2017), with a content of 0.01% out of the total 0.04% by mass (therefore this is not visible in Fig. 4).

3.1.3. Aggregate crushing value

Fig. 5 shows the measured aggregate crushing values (ACV) for M-slag, slag, glass, and refractory (i.e. the brittle classes) found in BA related to those of reference river quartz and limestone aggregates of correlating size fractions.

Overall, it can be seen that all materials show an increased ACV with an increase in particle size wherein all materials are influenced the same way. This effect can be related to the inherently lower amount of particles in the cylinder and the resulting higher void fraction for larger particles. In turn, an equal load is distributed over fewer particles causing a higher load per particle in combination with a larger available volume available to be filled by the fractured material. Furthermore, with the increase in particle size, a larger sieve size is prescribed by the standard (BS 812: Part 110, 1990), potentially adding to the crushing ACV.

To overcome this artefact, the ACV of the BA classes is correlated to the ACV of quartz and limestone fractions, shown in Fig. 6a and b, respectively. In general, all BA classes have a higher ACV and, therefore, lower resistance to crushing than the commonly applied quartz and limestone reference aggregates. The refractory fractions show the lowest ACV, followed by the M-slag, glass, and lastly slag. The relatively low ACV of the M-slag in comparison with the slag can be partially related to the presence of incorporated ferrous particles which are not prone to fracturing and will therefore not contribute to the ACV. Furthermore, in both Fig. 6a and b, it can be seen that the graph of the refractory and the M-slag show a matching slope and that graph of the glass and the slag also show an equal, yet steeper slope. Hence, refractory and M-slag are influenced equally by an increase in particle size, which also applies to glass and slag. The latter, however, are more prone to fracturing in the larger fractions. Additionally, in Fig. 6b it can be seen that the angle of the slope for refractory and M-slag approximates unity, indicating a crushing behaviour over the particle sizes which is closely related to that of the limestone aggregates. The indication that classes within the BA fracture distinctively different under the same conditions is encouraging for the potential to selectively crush materials and beneficiate fractions.

3.1.4. Specific density

The specific density can be used as a first indicator to detect when the composition of a specific size fraction changes since this feature is independent of particle shape, particle size, and open porosity. When a heterogeneous material consists of classes with
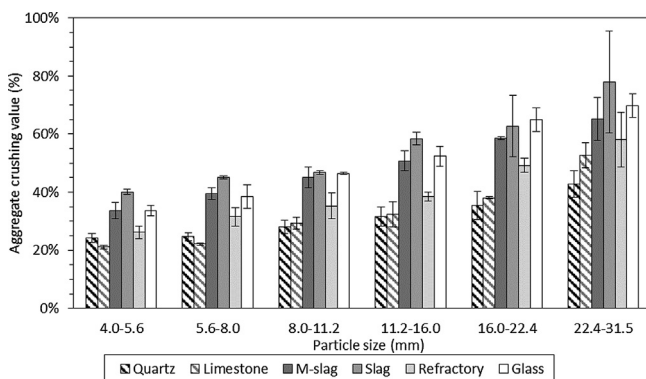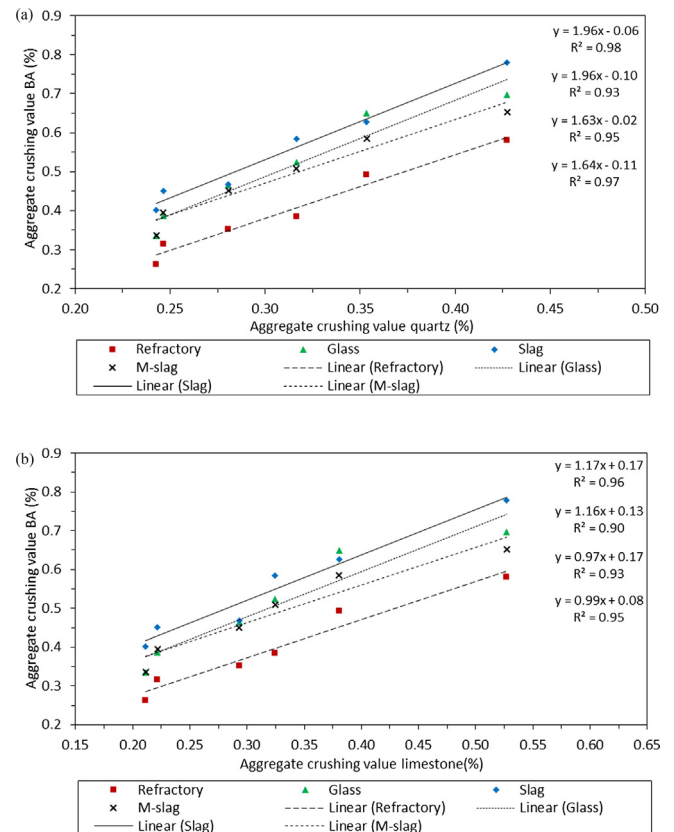

Fig. 6. Average aggregate crushing value of brittle BA constituents (M-slag, slag, refractory, and glass), related to the same size fraction of: a. Quartz, b. Limestone.

dissimilar densities, a variation in the ratio between these classes can result in a different overall specific density. This is always the case when the heterogeneity of the material is due to a combination of only two classes of different densities (e.g. hardened cement paste and aggregates). In the case of recycled concrete, this approach has been proven to work (Florea and Brouwers, 2013; van de Wouw et al., 2016).

Fig. 7 shows the specific densities related to the size fractions of the M-slag, slag, refractory, and glass classes, with weighted average densities of 3.07 g/cm³, 2.76 g/cm³, 2.79 g/cm³, and 2.51 g/cm³ respectively. Due to a low quantity, overall 0.1% by mass, the largest size fraction of glass (22.4–31.5 mm) is deemed to be not representative. Nevertheless, since the density of all glass size fractions is nearly constant at 2.51 g/cm³, this is extrapolated to
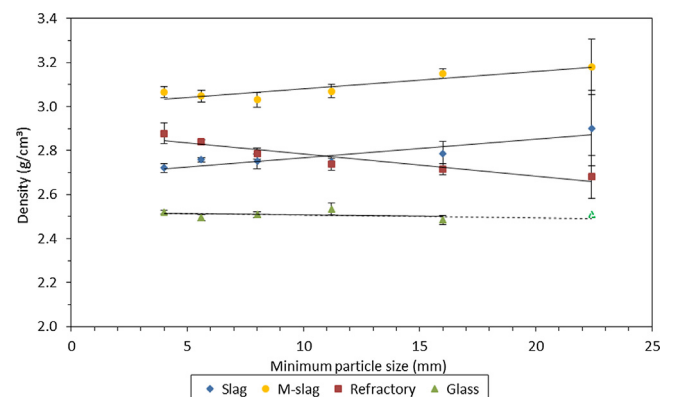

Fig. 5. Aggregate crushing value of brittle BA constituents (M-slag, slag, refractory, and glass), quartz, and limestone aggregates (including standard deviation) related to particle size.

Fig. 7. Specific density (including standard deviation) of milled MSWI BA classes fractions from BA 4–31.5 mm sieved to <125 μm related to particle size.

31.5 mm. For both the M-slag and slag classes, the density-particle size correlation shows the same trend with an increase in particle size. Additionally, M-slag shows an 11.3% (±1.3%) higher density than slag across all size fractions. The density of the refractory class is in the same range as that of the slag, however, the correlation is inverse with the particle size. In contrast to the other classes, glass has a constant and lower density. Therefore, density separation is considered feasible for the M-slag and glass classes, however, the small differences in some size fractions can obstruct a clean separation.

3.1.5. Mineralogical composition

Fig. 8 displays representative X-ray diffraction patterns for the different classes. All classes, including the presumed amorphous glass, show a presence of quartz. This common mineral is inert during incineration and either has a natural origin or derives from building materials where it is extensively applied (Alam et al., 2019b). Therefore, quantities of quartz are likely incorporated in (attached) slag or fused into the outer layer of glass (Müller and Rübner, 2006b) and stand out clearly from the amorphous background. The slag, M-slag, and refractory all show the presence of feldspar (natural minerals/incineration products), melilite, and pyroxene (incineration products) (Alam et al., 2019; Eighmy et al., 1994). Magnetite and wüstite found in M-slag can be formed in the vicinity of primary Fe-rich components (del Valle-Zermeño et al., 2017; Wei et al., 2017), whereas in the small fractions of refractory they can be included as pigment (Bondioli et al., 1998; Jordán et al., 1999), but not in slag indicating a successful magnetic separation (despite only magnetite being magnetic). In contrast to the other classes, only refractory shows appreciable amounts of amphibole, a refractory mineral (Wei et al., 2011a), and calcite ($CaCO_3$) which can be found in ceramic bricks and red roof tiles (Pacheco-Torgal and Jalali, 2010). From TG analysis, however, mass losses due to CO_2 release are found in the range of 0–2% for all classes except glass. Calcite is a weathering product and further carbonation can occur during sample preparation and storage, therefore, calcite cannot be attributed solely to the material (Alam et al., 2019b; Chimenos et al., 2000).

In addition to the fact that most of the minerals identified are present in multiple classes, amorphous content (not quantifiable with XRD) is known to make up a substantial quantity of the BA and can be seen throughout all classes (Eighmy et al., 1994; Eusden et al., 1999). Furthermore, identifiable minerals commonly found in BA (e.g. melilites, pyroxenes, etc.) can incorporate a wide

range of elements, making Rietveld refinement challenging. In turn, without Rietveld refinement, XRD does not provide sufficiently detailed information and is, therefore, found to be unsuitable for the determination of the class composition.

Through DSC analysis, the average quartz content of M-slag, slag, and refractory is quantified and found to be respectively 8.52% (±1.50%), 11.24% (±0.86%), and 11.34% (±2.71%). For the glass class, the presence of quartz seen in Fig. 8 could not be detected.

3.1.6. Oxide composition

Fig. 9a–d show ternary plots of the normalized oxide composition (obtained through XRF analysis) for the four main oxides (Al_2O_3, SiO_2, CaO, and Fe_2O_3) (Dhir et al., 2017) of the four separate classes (M-slag, slag, refractory, and glass). The concentration of Na_2O cannot be determined accurately in most samples because of the high detection limit of the instrument. Only pure glass contains sufficient equivalent Na_2O, however, mixed with other classes the amount falls below the detection limit and is, therefore, not represented.

In addition to the measured data points, the ternary plots show correlating compositions from literature. Overall, the derived data corresponds well with the measured data, especially for the SiO_2-CaO-Fe_2O_3 ternary diagram. Since limited data is available on BA class compositions, it is derived from electron microprobe analysis (EPMA) of vitrified BA (Bayuseno and Schmahl, 2010; Saffarzadeh et al., 2009a, 2009b, 2006), PhAse Recognition and Characterization (PARC) of BA (Alam et al., 2019b, 2019a; Schollbach et al., 2016), scanning electron microscopy/energy-dispersive X-ray spectroscopy (SEM/EDX) of BA (Wei et al., 2011a, 2011b), and XRF of non-incinerated glass and ceramics (Pacheco-Torgal and Jalali, 2010; Seward and Vascott, 2006; Wild et al., 1997). Hence, with the measured composition representing bulk compositions of individual batches, classes, and fractions, this can cause the deviation between the measured composition and literature. The ceramics show a broader range, attributable to the presence of magnetite and wüstite. The slag references (from pyrolysis) show a broader range indicative of low and high silica slags (critical boundary CaO/SiO_2 ~0.74–0.75) associated with the incinerator design and the melt chemistry (Saffarzadeh et al., 2009a, 2006). Prerequisites for the formation of low silica slag entail "intense melting, incipient crystallization of melilite and plagioclase, and extensive homogenization" (Saffarzadeh et al., 2009a). The presence of organics in the BA is a clear indication that these conditions are not met during incineration, in turn validating the presence of exclusively high silica slag.

It can be seen that for all classes (except refractory) the contents of the oxides are nearly equal throughout the various samples. Not only does this show that the manual separation is performed successfully, but it can also be concluded that through the various size fractions studied, especially for the glass, the oxide composition is nearly constant. The average oxide compositions of M-slag, slag, refractory, and glass are given in Table 1. Looking at the difference between the M-slag and slag classes, as expected, a clear difference between the Fe_2O_3 content can be observed (Fig. 9a, b, and d). With a CaO/SiO_2 ratio of 0.36 and 0.29 for M-slag and slag respectively, they are distinctly different from either refractory or glass, which have respective ratios of 0.17 and 0.14. The nearly equal Fe_2O_3 content throughout the particle size fractions seen in both the slag and the M-slag class (respectively ~7% and ~24%) correlates with the difference found in trends between their specific densities (Fig. 7). Compared to all other classes, the glass is found to be the most stable throughout the size fractions, containing a relatively high amount of SiO_2, together with low Al_2O_3 and Fe_2O_3 contents. For refractory, the reduction seen in the specific density with an increase in particle size can potentially be traced back to the reduction in the Fe_2O_3 content and an increase in SiO_2 and Al_2O_3.
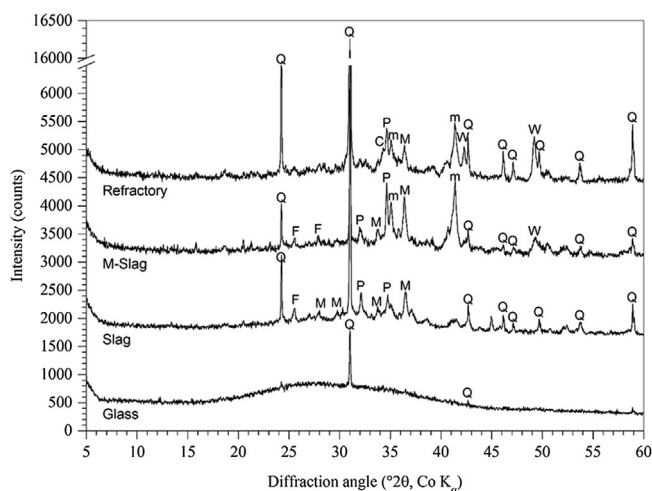

Fig. 8. Representative X-ray diffraction patterns of glass, slag, M-slag, and refractory. Q: quartz, M: melilite, P: pyroxene, m: magnetite, F: feldspar, C: calcite, W: wüstite.
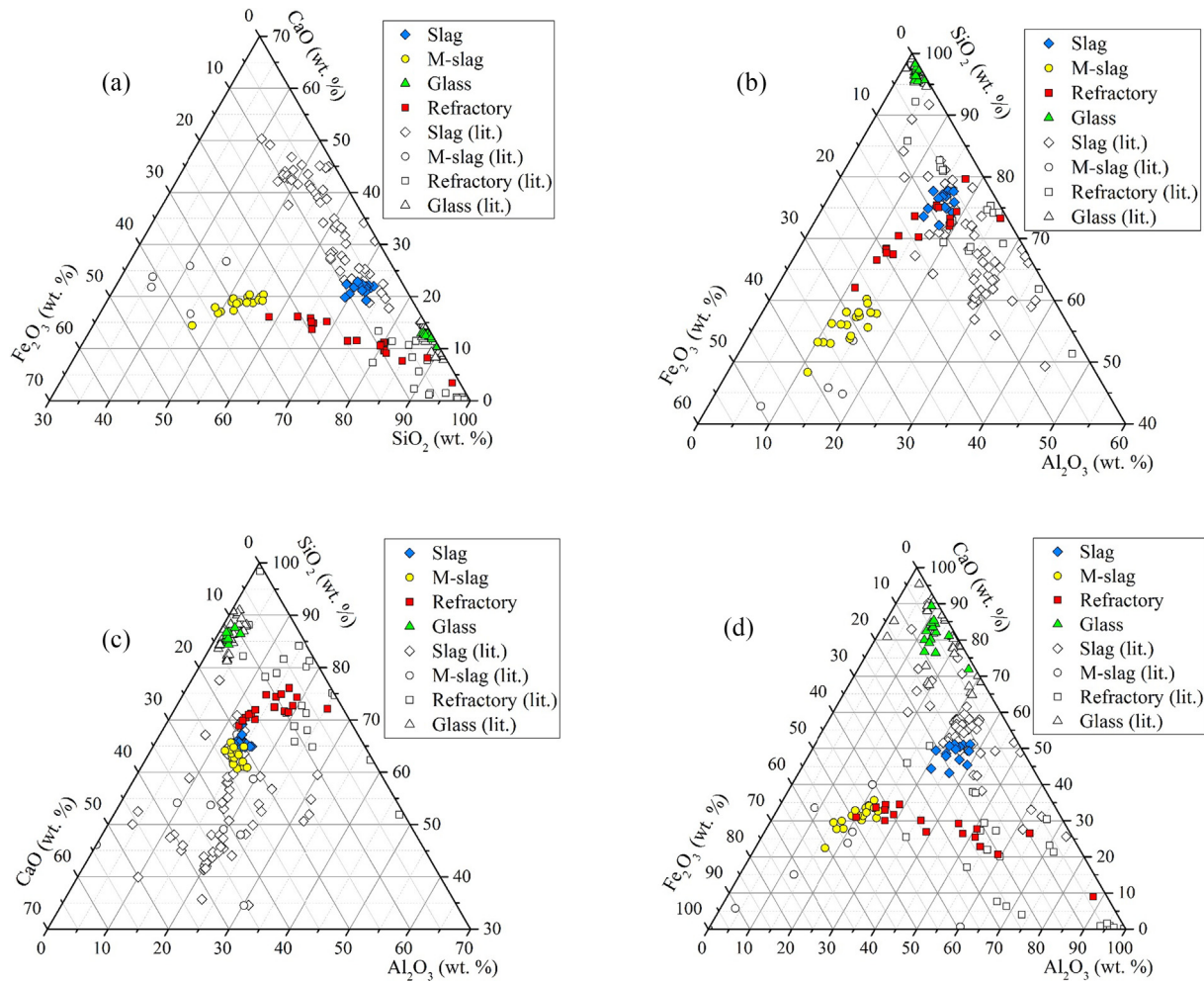
Fig. 9. Ternary plots of the normalized oxide composition for the main oxides from this study and from literature (Alam et al., 2019b, 2019a; Bayuseno and Schmahl, 2010; Pacheco-Torgal and Jalali, 2010; Saffarzadeh et al., 2009a, 2009b, 2006; Seward and Vascott, 2006; Wei et al., 2011a; Wild et al., 1997): a. SiO_2, CaO, and Fe_2O_3, b. Al_2O_3, SiO_2, and Fe_2O_3, c. Al_2O_3, SiO_2, and CaO, d. Al_2O_3, CaO, and Fe_2O_3.

Table 1
Average oxide composition of the M-slag, slag, refractory, and glass classes of BA obtained through XRF.

Compound	M-slag (wt%)	Slag (wt%)	Refractory (wt%)	Glass (wt%)
SiO_2	42.69	55.10	56.96	69.27
CaO	15.40	16.43	10.09	10.12
Fe_2O_3	22.55	5.72	11.67	0.70
Al_2O_3	10.35	11.78	12.27	1.58
Na_2O	0.79	1.52	0.27	14.14
MgO	2.23	2.52	1.49	1.55
P_2O_5	0.66	0.69	0.28	0.00
SO_3	0.73	0.41	0.35	0.15
K_2O	0.84	1.27	2.45	0.75
TiO_2	1.26	1.36	0.77	0.10
Cr_2O_3	0.12	0.08	0.06	0.05
NiO	0.03	0.02	0.01	0.00
CuO	0.32	0.39	0.13	0.04
ZnO	0.36	0.41	0.19	0.03
SrO	0.05	0.05	0.03	0.07
MoO_3	0.01	0.02	0.00	0.00
BaO	0.14	0.13	0.09	0.16
PbO	0.15	0.12	0.10	0.14
Cl	0.04	0.03	0.01	0.01
LOI	1.29	1.94	2.77	1.15

3.2. Application to initial BA

3.2.1. Particle size distribution

In order to quantify the influence of crushing on the particle size, for both the initial bottom ash 2.0–31.5 mm as well as for the fractions obtained after crushing, the PSD is determined. Fig. 10 shows the particle size distributions as both frequency and cumulative distribution, prior to and after crushing, on a logarithmic scale. Of the initial 2.0–31.5 mm MSWI BA, the dotted line in Fig. 10 shows the complete PSD, whereas the solid section of this line depicts the particle range used for the separation into classes. This 4–31.5 mm size range accounts for 82.3% by mass of the total material. It can be seen that a size reduction has taken place in which the top size of the material reduces from below 45.0 mm to below 22.4 mm. Despite that most of the material remains in the 5.6–8.0 mm fraction, the peak of the particle frequency lowers and broadens, whereby the newly formed particles in the 63 μm– 1.4 mm size range are evenly distributed.

3.2.2. Specific density

In order to detect changes, prior to and after crushing the specific density is measured for all size fractions individually (Fig. 11). The largest size fraction (11.2–16.0 mm) of the crushed BA was present in a low mass percentage and therefore considered to not be representative.

After crushing, 13 out of the 17 remaining size fractions show an increased density, while the remaining few size fractions show a lowered density. In contrast to a two-component heterogeneous material, in a multi-class material (e.g. BA) different combinations of classes (see Fig. 7) can result in an equal density measured. Consequently, in this case, the specific density is not conclusive regarding the composition and is, therefore, not suitable as a tracer for the composition of classes.

3.2.3. Oxide composition

As with the separated classes, the oxide composition of the overall BA and that of the smallest and the largest fractions of both the initial and the crushed BA are given in Table 2. Clearly, the crushing of the BA has an influence on the composition of these fractions. Metals (2.8% by mass) and unburned organic materials (0.04% by mass) are omitted.

For the remaining fractions, the oxide compositions for the initial BA fractions are presented for their four main oxides (Al_2O_3, SiO_2, CaO, and Fe_2O_3) in Fig. 12a. Here it can be seen that the various size fractions show a wide range in their oxide composition

with only a relatively stable composition in the fines <125 μm and in the fraction range from 5.6 mm to 11.2 mm. This indicates that the content of the classes over the other size fractions has a large variation. The particles smaller than 180 μm show a remarkably distinct oxide composition (Al_2O_3 and Fe_2O_3 ~26% each; SiO_2 and CaO ~17% each). Neither the high CaO content nor the low SiO_2 content can be correlated to the individual classes distinguished. TG analysis indicates that only a small quantity of the CaO detected in the XRF analysis can be attributed to the presence of $Ca(OH)_2$ and $CaCO_3$, materials commonly found in BA. Calcite is found to accumulate in the finest size fractions (Alam et al., 2019b), which corresponds to the lower CaO content detected in the larger size fractions.

Accordingly, particles larger than 125 μm that remained after milling were extracted prior to making the fused beads. As with the individual classes and the initial BA, the oxide compositions are presented for the four main oxides (Al_2O_3, SiO_2, CaO, and Fe_2O_3) in Fig. 12b. In comparison with the size fractions prior to crushing (Fig. 12a and b), it can be seen that the distribution of the crushed BA is more even over the various size fractions. Three distinct groups can be identified within the various size ranges generated. Once more, the fractions finer than 125 μm show similar oxide compositions. The fractions from 125 μm to 4.0 mm show relatively stable levels of CaO and Al_2O_3 together with a steady increase in Fe_2O_3 content and a reduction of the SiO_2 content with an increase in particle size. The particles found in the 4.0 mm to 22.4 mm size range show a larger, yet similar deviation in oxide composition compared to those of the largest size fractions of the initial BA. When the cumulative weighted composition of both the initial BA and the crushed are compared, the total deviation between initial and crushed BA are respectively +0.1%, +1.0%, −0.6% and −0.5% for Al_2O_3, SiO_2, CaO, and Fe_2O_3 confirming a balance in oxides prior to and after crushing.

Based on this data it can be concluded that through jaw crushing, the composition of the BA in the 125 μm to 4.0 mm size fraction becomes more homogeneous. The particles larger than 4.0 mm of the initial BA correlate to those found in the largest size fractions of the crushed BA, indicating that these materials possess a higher resistance to crushing under the considered conditions. These fractions can be identified as a predominantly refractory material, having the lowest crushing value (Fig. 5) and the most comparable oxide composition (Fig. 9a–d) of the classes.

3.3. Compositional model

In order to be able to quantify the magnitude of the 4 material classes in BA fractions and track classes over the crushing process, a model based just on the content of SiO_2, CaO, and Fe_2O_3 is presented. Ideally, a chemical tracer belonging to only one class would be used, however, none of the major, nor the minor oxides is exclusive to any of the classes, therefore, no distinct chemical tracer could be identified. E.g. Na_2O, predominantly present in glass (13.1–17.2%), is also present in feldspars (0.0–12.0%) (Greenwood and Earnshaw, 1997) and in the slag classes (0.0–3.6%). Hence, a mathematical fit is used instead. The assumption was made that an entire BA sample can be characterised by the four major oxide groups, namely: SiO_2, CaO, Fe_2O_3 and residual oxides, normalised to 100%. The same was assumed for the classes comprising a BA sample, so the entire sample is presumed to only consist of 4 different classes. Hence, three classes are independent whereby the fourth class is determined by a total of 100%. A principal component analysis of all oxide compositions of the separated materials indicates CaO, Fe_2O_3, and SiO_2 to account for the most variance in the data, followed by Na_2O and Al_2O_3. Additionally, Na_2O is not chosen due to the high detection limit of the instrument which does not allow for reliable use of this oxide in low concentrations.
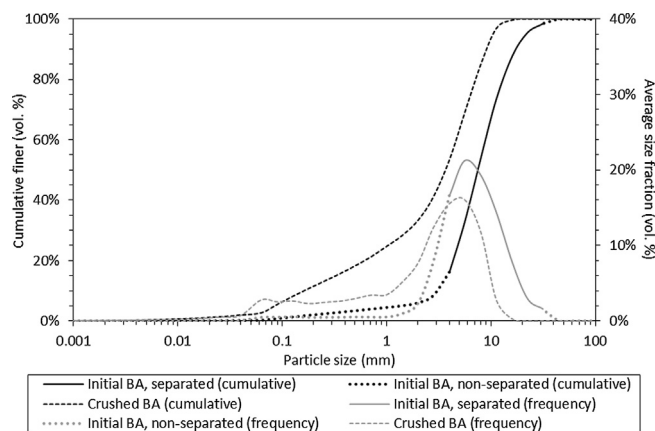

Fig. 10. Mean particle size distributions of the initial 2.0–31.5 mm MSWI BA (solid lines indicate the fractions used for manual separation) and the jaw-crushed MSWI BA.
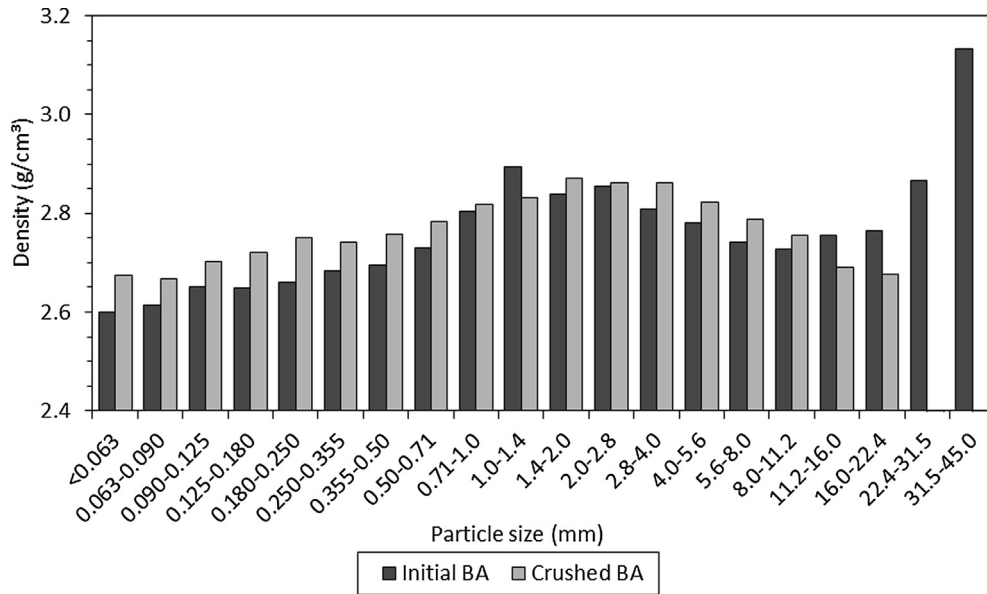
Fig. 11. The average specific density of initial and crushed BA size fractions.

Table 2
Oxide composition of the total BA, initial BA (fraction <63 μm and 22.4–31.5 mm), and crushed BA (fraction <63 μm and 16.0–22.4 mm) obtained through XRF.

Compound	Total BA (wt%)	Initial BA <63 μm (wt%)	Initial BA 22.4–31.5 mm (wt%)	Crushed BA <63 μm (wt%)	Crushed BA 16.0–22.4 (wt%)
SiO_2	53.23	29.85	50.97	43.74	64.13
CaO	12.60	17.30	11.69	14.96	3.09
Fe_2O_3	12.52	10.04	10.60	9.93	2.86
Al_2O_3	10.22	14.48	13.54	13.52	23.48
Na_2O	3.68	0.00	0.00	1.75	0.00
MgO	1.88	1.63	1.18	1.93	1.85
P_2O_5	0.40	0.73	0.33	0.58	0.00
SO_3	0.56	3.32	0.26	1.70	0.00
K_2O	0.97	0.86	1.23	1.03	3.02
TiO_2	0.90	0.93	0.99	0.88	0.49
Cr_2O_3	0.09	0.09	0.05	0.08	0.02
NiO	0.02	0.04	0.01	0.03	0.01
CuO	0.29	0.52	0.19	0.41	0.01
ZnO	0.25	0.84	0.26	0.52	0.05
SrO	0.05	0.05	0.03	0.05	0.02
BaO	0.01	0.01	0.25	0.00	0.00
PbO	0.13	0.12	0.04	0.13	0.05
Cl	0.13	0.19	0.01	0.14	0.01
LOI	1.86	0.13	5.16	0.18	0.00

Furthermore, a comparison of the XRF results with ICP analysis of the totally digested fused beads has shown to correlate best for SiO_2, CaO, and Fe_2O_3. With Al being the lightest element of these four major oxides, Al_2O_3 has shown to be the least reliable and is therefore not used either as an independent variable (Loginova et al., 2017). Additionally, all 22.4–31.5 mm fractions, in total less than 3% of the initial BA by mass (Fig. 10), are excluded due to a comparably small sample size and large variation in oxide composition. Hence, a total of 60 bulk samples (3 batches, 5 fractions, 4 classes) were used in the model.

The distribution of the classes that make up a heterogeneous BA fraction can be determined mathematically through its overall oxide composition. By relating this to the oxide compositions of the individual classes (Fig. 9a–d), their rate of occurrence can be calculated. The following equations describe the algorithm for computing the configuration of the brittle classes of a heterogeneous BA sample using the oxide content of the individual classes (Table 3):

$$y_{Si} = x_{ms} * z_{Si,ms} + x_s * z_{Si,s} + x_r * z_{Si,r} + x_g * z_{Si,g} \quad (1)$$

$$y_{Ca} = x_{ms} * z_{Ca,ms} + x_s * z_{Ca,s} + x_r * z_{Ca,r} + x_g * z_{Ca,g} \quad (2)$$

$$y_{Fe} = x_{ms} * z_{Fe,ms} + x_s * z_{Fe,s} + x_r * z_{Fe,r} + x_g * z_{Fe,g} \quad (3)$$

$$y_{RO} = x_{ms} * z_{RO,ms} + x_s * z_{RO,s} + x_r * z_{RO,r} + x_g * z_{RO,g} \quad (4)$$

where

$$0\% \leq x_{ms}, x_s, x_r, x_g \leq 100\% \quad (5)$$

y_{Si}, y_{Ca}, y_{Fe}, and y_{RO} are the measured oxide concentrations of a BA sample (for SiO_2, CaO, Fe_2O_3 and residual oxides respectively), normalised to 100%, and x_{ms}, x_s, x_r, and x_g are the contents of the classes (for M-slag, slag, refractory, and glass respectively), in total 100%, and $z_{S,ms}$, $z_{S,s}$, $z_{S,r}$, and $z_{S,g}$ are the average SiO_2 contents, $z_{C,ms}$, $z_{C,s}$, $z_{C,r}$, and $z_{C,g}$ are the average CaO contents, $z_{F,ms}$, $z_{F,s}$, $z_{F,r}$, and $z_{F,g}$ are the average Fe_2O_3 contents, and $z_{RO,ms}$, $z_{RO,s}$, $z_{RO,r}$, and $z_{RO,g}$ are
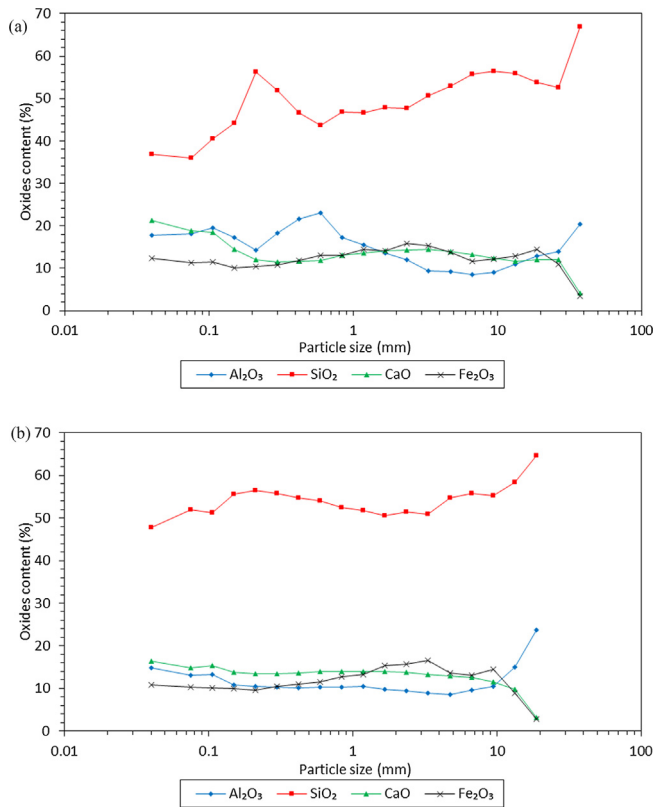
Fig. 12. Average XRF-obtained Al₂O₃, SiO₂, CaO, and Fe₂O₃ content of: a. Initial BA, b. Jaw crushed (CSS 8 mm) BA.

Fig. 13. Computed composition related to the composition found (including standard deviation) through separation for the brittle classes (M-slag, slag, refractory, and glass) of the 4–11.2 mm fraction.

the average residual oxide contents of respectively M-slag, slag, refractory, and glass as given in Table 3.

The 4.0–22.4 mm classes (M-slag, slag, refractory, and glass) can be separated and their oxide composition determined. To determine the amount of each class in the finer size fractions and the fractions generated after crushing, the oxide compositions of the separated 4.0–22.4 mm fractions are employed. As can be seen in Fig. 10, in addition to the original fines, the majority of the finer particles present after the jaw crushing process originates from the brittle classes (e.g. M-slag and slag) found in the larger initial BA fractions.

3.3.1. Validation

The configuration of the classes found by separating the 3 predominant fractions (4.0–11.2 mm) of three independent sets (Fig. 4), making up 57.2% (±1.5%) of the complete BA by mass, were used as validation sets for the algorithm. Fig. 13 shows this mean composition related to the mean composition computed by the model based on 3 separate batches, each involving 3 fractions in the 4.0–11.2 mm size range.

As can be seen in Fig. 13, the mean composition of the total 4.0–11.2 mm fraction, a size range commonly used in practice, lies
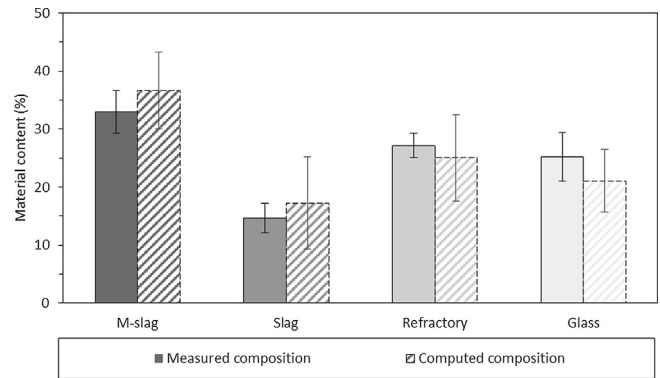
within the standard deviation (σ), an acceptable deviation considering the spread in class composition.

With the calculated ratio of classes for each individual fraction and the measured quartz content of the individual classes, the theoretical quartz content of each fraction is calculated. Fig. 14a and b depict both the measured and the calculated quartz content for the initial BA and the crushed BA fractions, respectively. For the initial BA and the crushed BA it can be seen that, with an average deviation of respectively 1.79% and −0.19%, a standard deviation of respectively 4.19% and 2.27%, and a maximum deviation of respectively 10.34% and −4.76%, the calculated quartz content is close to the measured content. For the initial BA a larger deviation between calculated and measured quartz content can be seen for the fractions <500 μm (3.00% of the total material), this larger deviation is likely due to the presence of materials other than the classes. The values for the crushed BA, however, are closely related over all fractions. As with the oxide composition, also here, a more homogeneous distribution can be seen after jaw crushing.

The material classes can be visually differentiated for the larger particle fractions, resulting in classes being clean, consistent to themselves, and to literature (Fig. 9a). Using the acquired composition and the proposed method, the material classes can also be quantified for the related finer fraction (<4 mm). Furthermore, the literature consistency indicates its applicability to any bottom ash that can be assumed to have just these classes (no significant metals or unburnt), regardless of its actual XRF composition. A low fit would inherently indicate other classes present.

3.3.2. Computed crushing curves

Applying the model to the oxide compositions gives the distribution of classes over the fractions. To a lesser degree than with the initial BA, the crushed BA also has fractions which cannot be fully covered by the model (<63 μm and >16.0 mm). The deviation in oxide composition is given in Table 3 as well. The calculated distribution of the classes for both the initial and crushed BA fractions is presented in Fig. 15a and b for both the cumulative and the sieve fraction.

Table 3
Oxide content used in the algorithm for the three most reliable and distinct major compounds.

Classes		Oxide composition (wt%)				Total
		SiO₂ (Z_S)	CaO (Z_C)	Fe₂O₃ (Z_F)	Residual (Z_{RO})	
M-slag	($_{ms}$)	42.59	15.26	22.9	19.25	100
Slag	($_s$)	55.60	16.36	5.71	22.33	100
Refractory	($_r$)	57.27	9.97	11.63	21.13	100
Glass	($_g$)	69.11	9.81	0.63	20.45	100
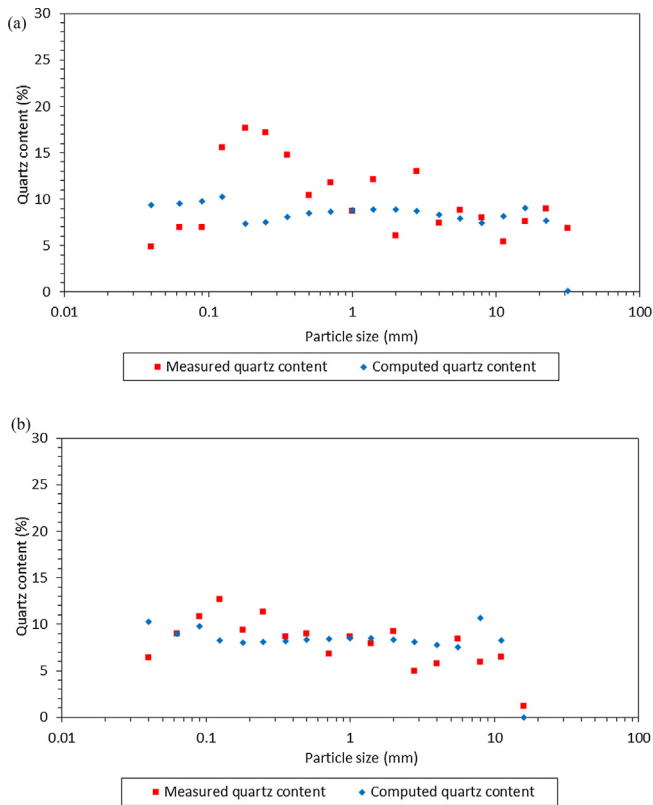
Fig. 14. Mean measured and computed quartz content of a. Initial MSWI BA 2.0–31.5 mm, b. Crushed BA.

Fig. 15. Average cumulative (solid) and non-cumulative (dashed) computed configuration of classes of a. Initial MSWI BA 2.0–31.5 mm, b. Crushed BA.

Fig. 16. The average change in class configuration due to crushing expressed in mass percent.

Apart from the reduction in the top size of the material, a clear difference in the distribution of the various classes can be seen. Each class shows a distinct depletion and depositing over the size ranges (Fig. 16). Slag and M-slag are found to be present in the finer fractions of which the content increases after crushing in correlation with their determined crushing values (Fig. 5 and Fig. 6a and b). The near absence of refractory in the fractions <125 μm correlates to the higher crushing resistance of this class. Originally, both the glass and the refractory classes have a relatively narrow distribution which is found to be extended after the crushing. With a slightly higher content of glass than refractory, both materials show a constant content in the 125 μm–1.4 mm size fraction. Furthermore, despite its lower specific density, it can be seen that the refractory class is mostly present in the larger size fractions, correlating to its lower crushing value and its beneficiation in these fractions.

When comparing the computed cumulative composition for each individual class prior to and after crushing, a decrease in the total content of 5.7% and 4.1% for glass and refractory respectively and an increase of 2.7% and 7.1% for M-slag and slag respectively can be observed. Since multi-class particles (e.g. slag melted on a glass particle) have been classified by their predominantly present material, besides measurement uncertainty, this deviation can be attributed to the liberation of glass and refractory from slag particles during crushing.

4. Conclusions and recommendations

In this article, material classes in the different size fractions are identified and defined, their individual properties determined, a practical tracer for material class tracking determined, a user-friendly 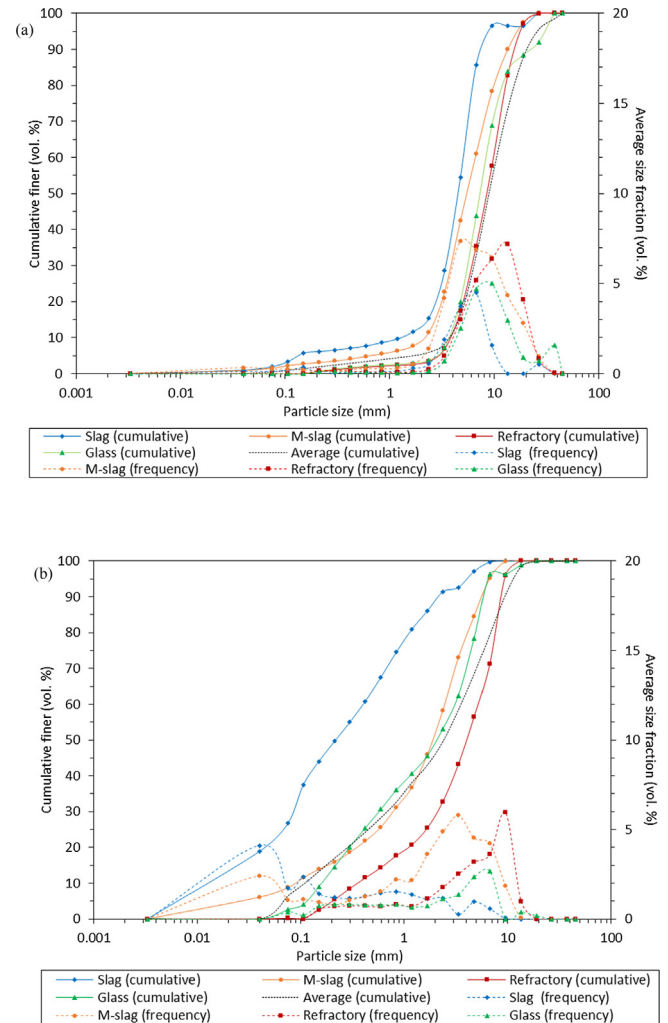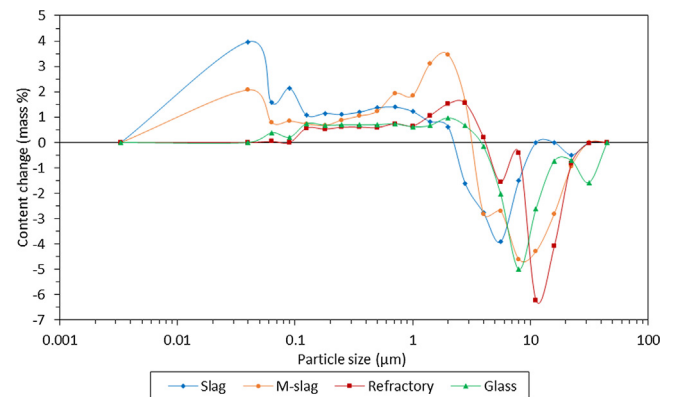method to quantify the distribution of material classes over the size fractions developed, and with this, the changing composition through crushing approximated.

- BA can be categorised into distinct applicability influencing material classes, namely: slag, refractory, glass, metals, and unburned matter. XRF analysis indicated that hand-separation

is an effective yet capacity-inefficient technique to separate a 4–31.5 mm BA into these classes. Additionally, 70% of the slag is found to be extractable by a magnet, accounting for 32.5% of the overall bottom ash. Hereby, magnetic separation has the potential to provide cleaner streams of M-slag and predominantly refractory, glass, and slag.

- Despite being higher, the aggregate crushing value (ACV) of refractory, and M-slag are equally influenced by particle size as the reference material limestone, while glass and slag are more prone to fracturing in the larger size fractions. The material-dependent fracturing indicates that beneficiation through the selective crushing of each of these material classes is possible.

- M-slag uniformly shows an 11.3% (±1.3%) higher specific density than slag, increasing with particle size. The densities of the refractory size fractions are inverse of those of slag, while glass shows a constant and overall lower density. M-slag, slag, refractory, and glass respectively show average densities of 3.07 g/cm^3, 2.76 g/cm^3, 2.79 g/cm^3, and 2.51 g/cm^3. Therefore, density is unsuitable as a tracer for the material class composition. However, a density-based separation of M-slag and glass classes seems possible, yet challenging.

- Multiple classes of materials contain quartz, melilite, pyroxene, magnetite, and feldspar, whereas only calcite and amphibole are exclusive to the refractory class. Additionally, the amorphous content cannot be quantified, disqualifying XRD analysis for the determination of the material class composition.

- XRF analysis indicates a narrow spread in the oxide composition of the glass, M-slag, and slag classes, whereas the refractory class shows a bigger spread related to the variance in materials making up this class. Nevertheless, the ratios between SiO_2, CaO, Fe_2O_3, and residual oxides are distinctive for each individual material class consistent to themselves and to literature, enabling its use for calculation of the composition of material classes.

- A model, based just on the content of SiO_2, CaO, and Fe_2O_3, to calculate the content of the various brittle classes comprising a BA size fraction is proposed and validated. With the larger particle fractions, the material classes could be distinguished visually. Using the proposed method, also for the small fraction (<4 mm), the material classes can be quantified.

- After the removal of metals and unburned organics, most bottom ash compositions, regardless of origin, are expected to benefit from the proposed model for material classes quantification.

- Application of this method has shown that, through jaw crushing, the distribution of material classes becomes noticeably more homogeneous. Nevertheless, three distinct fractions can be perceived, indicating partial beneficiation: a fine fraction (<125 μm) of predominantly slag and M-slag, a homogeneous sand fraction (125 μm–4.0 mm), and a gravel size fraction (<4 mm) which is enriched in refractory materials.

In practice, the proposed characterisation method can be applied to determine the composition of classes of materials making up a BA fraction in order to: quantify and optimise the effect of a crushing treatment (e.g. beneficiation), determine the effect of physical separation techniques, monitor the composition of produced output materials, and predict the behaviour of a BA fraction prior to use.

Future work will include the extension of the model to different incinerators and various degrees of pre-processing. As well as studying the influence of crushing parameters to the fracturing of material classes, the quantification of the crushing curves in correlation with the model, and the beneficiation of material classes into size fractions for better application and isolation of the contaminated fraction.

References

Al-Rawas, A.A., Wahid Hago, A., Taha, R., Al-Kharousi, K., 2005. Use of incinerator ash as a replacement for cement and sand in cement mortars. Build. Environ. 40, 1261–1266. https://doi.org/10.1016/j.buildenv.2004.10.009.

Alam, Q., Florea, M.V.A., Schollbach, K., Brouwers, H.J.H., 2017. A two-stage treatment for Municipal Solid Waste Incineration (MSWI) bottom ash to remove agglomerated fine particles and leachable contaminants. Waste Manag. 67, 181–192. https://doi.org/10.1016/J.WASMAN.2017.05.029.

Alam, Q., Schollbach, K., Rijnders, M., van Hoek, C., van der Laan, S., Brouwers, H.J.H., 2019a. The immobilization of potentially toxic elements due to incineration and weathering of bottom ash fines. J. Hazard. Mater. 379, 120798. https://doi.org/10.1016/j.jhazmat.2019.120798.

Alam, Q., Schollbach, K., van Hoek, C., van der Laan, S., de Wolf, T., Brouwers, H.J.H., 2019b. In-depth mineralogical quantification of MSWI bottom ash phases and their association with potentially toxic elements. Waste Manag. 87, 1–12. https://doi.org/10.1016/j.wasman.2019.01.031.

Allegrini, E., Vadenbo, C., Boldrin, A., Astrup, T.F., 2015. Life cycle assessment of resource recovery from municipal solid waste incineration bottom ash. J. Environ. Manage. 151, 132–143. https://doi.org/10.1016/j.jenvman.2014.11.032.

Arickx, S., Van Gerven, T., Knaepkens, T., Hindrix, K., Evens, R., Vandecasteele, C., 2007. Influence of treatment techniques on Cu leaching and different organic fractions in MSWI bottom ash leachate. Waste Manag. 27, 1422–1427. https://doi.org/10.1016/j.wasman.2007.03.015.

Arickx, S., Van Gerven, T., Vandecasteele, C., 2006. Accelerated carbonation for treatment of MSWI bottom ash. J. Hazard. Mater. 137, 235–243. https://doi.org/10.1016/j.jhazmat.2006.01.059.

Bayuseno, A.P., Schmahl, W.W., 2010. Understanding the chemical and mineralogical properties of the inorganic portion of MSWI bottom ash. Waste Manag. 30, 1509–1520. https://doi.org/10.1016/j.wasman.2010.03.010.

Bertolini, L., Carsana, M., Cassago, D., Quadrio Curzio, A., Collepardi, M., 2004. MSWI ashes as mineral additions in concrete. Cem. Concr. Res. 34, 1899–1906. https://doi.org/10.1016/j.cemconres.2004.02.001.

Biganzoli, L., Ilyas, A., van Praagh, M., Persson, K.M., Grosso, M., 2013. Aluminium recovery vs. hydrogen production as resource recovery options for fine MSWI bottom ash fraction. Waste Manag. 33, 1174–1181. https://doi.org/10.1016/j.wasman.2013.01.037.

Bondioli, F., Ferrari, A., Leonelli, C., Manfredini, T., 1998. Syntheses of Fe2O3/silica red inorganic inclusion pigments for ceramic applications. Mater. Res. Bull. 33, 723–729. https://doi.org/10.1016/S0025-5408(98)00047-6.

BS 812: Part 110, 1990. Testing Aggregates - Part 110: Methods for Determination of Aggregate Crushing Value (ACV). BSI.

CEWEP, 2017. Overview of landfill taxes and bans [WWW Document]. URL http://www.cewep.eu (accessed 1.25.18).

CEWEP, 2015. Bottom Ash Factsheet [WWW Document]. URL http://www.cewep.eu (accessed 2.15.18).

CEWEP, 2014. Country Report 2012-2013 The Netherlands.

Chandler, A.J., Eighmy, T.T., Hartlén, J., Hjelmar, O., Kosson, D.S., Sawell, S.E., van der Sloot, H.A., Vehlow, J., 1997. Municipal Solid Waste Incinerator Residues. Stud. Environ. Sci.

Cheng, A., 2012. Effect of incinerator bottom ash properties on mechanical and pore size of blended cement mortars. Mater. Des. 36, 859–864. https://doi.org/10.1016/j.matdes.2011.05.003.

Chimenos, J., Fernández, A., Nadal, R., Espiell, F., 2000. Short-term natural weathering of MSWI bottom ash. J. Hazard. Mater. 79, 287–299. https://doi.org/10.1016/S0304-3894(00)00270-3.

Chimenos, J.M., Segarra, M., Fernández, M.A., Espiell, F., 1999. Characterization of the bottom ash in municipal solid waste incinerator. J. Hazard. Mater. 64, 211–222. https://doi.org/10.1016/S0304-3894(98)00246-5.

Cioffi, R., Colangelo, F., Montagnaro, F., Santoro, L., 2011. Manufacture of artificial aggregate using MSWI bottom ash. Waste Manag. 31, 281–288. https://doi.org/10.1016/j.wasman.2010.05.020.

Cossu, R., Lai, T., Pivnenko, K., 2012. Waste washing pre-treatment of municipal and special waste. J. Hazard. Mater. 207–208, 65–72. https://doi.org/10.1016/j.jhazmat.2011.07.121.

Dabo, D., Badreddine, R., De Windt, L., Drouadaine, I., 2009. Ten-year chemical evolution of leachate and municipal solid waste incineration bottom ash used in a test road site. J. Hazard. Mater. 172, 904–913. https://doi.org/10.1016/j.jhazmat.2009.07.083.

del Valle-Zermeño, R., Formosa, J., Chimenos, J.M., Martínez, M., Fernández, A.I., 2013. Aggregate material formulated with MSWI bottom ash and APC fly ash for use as secondary building material. Waste Manag. 33, 621–627. https://doi.org/10.1016/j.wasman.2012.09.015.

del Valle-Zermeño, R., Gómez-Manrique, J., Giro-Paloma, J., Formosa, J., Chimenos, J.M., 2017. Material characterization of the MSWI bottom ash as a function of particle size. Effects of glass recycling over time. Sci. Total Environ. 581–582, 897–905. https://doi.org/10.1016/J.SCITOTENV.2017.01.047.

Dhir, R.K., de Brito, J., Lynn, C.J., Silva, R.V., 2017. Sustainable Construction Materials: Municipal Incinerated Bottom Ash, Sustainable Construction Materials: Municipal Incinerated Bottom Ash. Elsevier.

Dutch Soil Quality Decree, 2007. Regulation of the State Secretary for Housing, Planning and the Environment and the State Secretary for Transport, Public Works and Water Management, The Netherlands. Staatscourant nr. 469, 3 December 2007.

Eighmy, T.T., Eusden, J.D., Marsella, K., Hogan, J., Domingo, D., Krzanowski, J.E., Stämpfli, D., 1994a. Particle Petrogenesis and speciation of elements in MSW incineration bottom ashes. Stud. Environ. Sci. 60, 111–136. https://doi.org/10.1016/S0166-1116(08)71452-3.

van Eijk, R.J., 2001. Hydration of Cement Mixtures Containing Contaminants. Ipskamp BV, Enschede, The Netherlands.

EN 196-2, 2013. Method of testing cement - Part 2: Chemical analysis of cement. CEN.

EN 932-1, 1996. Tests for general properties of aggregates - Part 1: Methods for sampling.

EN 932-2, 1999. Tests for general properties of aggregates - Part 2: Methods for reducing laboratory samples.

EN 933-1, 2012. Tests for geometrical properties of aggregates - Part 1: Determination of particle size distribution - Sieving method. CEN.

EN 933-2, 1995. Tests for geometrical properties of aggregates - Part 2: Determination of particle size distribution - Test sieves, nominal sizes of apertures. CEN.

Eusden, J.D., Eighmy, T.T., Hockert, K., Holland, E., Marsella, K., 1999. Petrogenesis of municipal solid waste combustion bottom ash. Appl. Geochem. 14, 1073–1091. https://doi.org/10.1016/S0883-2927(99)00005-0.

Fayed, M.E., Otten, L., 1997. Handbook of Powder Science & Technology, second ed. Springer US, Boston, MA. http://doi.org/10.1007/978-1-4615-6373-0.

Ferraris, M., Salvo, M., Ventrella, A., Buzzi, L., Veglia, M., 2009. Use of vitrified MSWI bottom ashes for concrete production. Waste Manag. 29, 1041–1047. https://doi.org/10.1016/j.wasman.2008.07.014.

Florea, M.V.A., 2014. Secondary materials in cement-based products, Treatment, modelling and environmental interaction, Thesis, Eindhoven University of Technology. Eindhoven University of Technology.

Florea, M.V.A., Brouwers, H.J.H., 2012. Recycled concrete fines and aggregates: the composition of various size fractions related to crushing history. In: Proceedings of the 18th International Conference on Building Materials (IBAUSIL 2012). Weimar, Germany, 12–15 September 2012, pp. 1034–1041.

Florea, M.V.A., Brouwers, H.J.H., 2013. Properties of various size fractions of crushed concrete related to process conditions and re-use. Cem. Concr. Res. 52, 11–21. https://doi.org/10.1016/j.cemconres.2013.05.005.

Florea, M.V.A., Ning, Z., Brouwers, H.J.H., 2014. Activation of liberated concrete fines and their application in mortars. Constr. Build. Mater. 50, 1–12. https://doi.org/10.1016/j.conbuildmat.2013.09.012.

Florea, M.V.A., Quaas, L.C., Brouwers, H.J.H., 2016. MSWI by-products and immobilisates as concrete constituents. In: Schmidt, W., Msinjili, N.S. (Eds.), Proceedings of the 2nd International Conference on Advances in Cement and Concrete Technology in Africa (ACCTA). BAM Federal Institute for Materials Research and Testing, Berlin, Dar es Salaam, Tanzania, 27–29 January 2016, pp. 295–299.

Fontseré Obis, M., Germain, P., Bouzahzah, H., Richioud, A., Benbelkacem, H., 2017. The effect of the origin of MSWI bottom ash on the H2S elimination from landfill biogas. Waste Manag. 70, 158–169. https://doi.org/10.1016/J.WASMAN.2017.09.014.

Greenwood, N.N., Earnshaw, A., 1997. Chemistry of Elements.

Grosso, M., Biganzoli, L., Rigamonti, L., 2011. A quantitative estimate of potential aluminium recovery from incineration bottom ashes. Resour. Conserv. Recycl. 55, 1178–1184. https://doi.org/10.1016/j.resconrec.2011.08.001.

Hansen, T.C., 1992. Recycling of Demolished Concrete and Masonry. Spon, London.

Holm, O., Simon, F.-G., 2017. Innovative treatment trains of bottom ash (BA) from municipal solid waste incineration (MSWI) in Germany. Waste Manag. 59, 229–236. https://doi.org/10.1016/j.wasman.2016.09.004.

Hyks, J., Nesterov, I., Mogensen, E., Jensen, P.A., Astrup, T., 2011. Leaching from waste incineration bottom ashes treated in a rotary kiln. Waste Manag. Res. 29, 995–1007. https://doi.org/10.1177/0734242X11417490.

Inkaew, K., Saffarzadeh, A., Shimaoka, T., 2016. Modeling the formation of the quench product in municipal solid waste incineration (MSWI) bottom ash. Waste Manag. 52, 159–168. https://doi.org/10.1016/J.WASMAN.2016.03.019.

Inkaew, K., Saffarzadeh, A., Shimaoka, T., 2015. Impacts of water quenching on MSWI bottom ash characterization.

Jordán, M., Boix, A., Sanfeliu, T., de la Fuente, C., 1999. Firing transformations of cretaceous clays used in the manufacturing of ceramic tiles. Appl. Clay Sci. 14, 225–234. https://doi.org/10.1016/S0169-1317(98)00052-0.

Juric, B., Hanzic, L., Ilić, R., Samec, N., 2006. Utilization of municipal solid waste bottom ash and recycled aggregate in concrete. Waste Manag. 26, 1436–1442. https://doi.org/10.1016/j.wasman.2005.10.016.

Keulen, A., Florea, M.V.A., Brouwers, H.J.H., 2012. Upgrading MSWI bottom ash as building material for concrete mixes. In: Proceedings of the 18th International Conference on Building Materials (IBAUSIL 2012). Weimar, Germany, 12–15 September 2012, pp. 545–553.

Keulen, A., van Zomeren, A., Harpe, P., Aarnink, W., Simons, H.A.E., Brouwers, H.J.H., 2016. High performance of treated and washed MSWI bottom ash granulates as natural aggregate replacement within earth-moist concrete. Waste Manag. https://doi.org/10.1016/j.wasman.2016.01.010.

Li, X.-G., Lv, Y., Ma, B.-G., Chen, Q.-B., Yin, X.-B., Jian, S.-W., 2012. Utilization of municipal solid waste incineration bottom ash in blended cement. J. Clean. Prod. 32, 96–100. https://doi.org/10.1016/j.jclepro.2012.03.038.

Lin, K.L., Lin, D.F., 2006. Hydration characteristics of municipal solid waste incinerator bottom ash slag as a pozzolanic material for use in cement. Cem. Concr. Compos. 28, 817–823. https://doi.org/10.1016/j.cemconcomp.2006.03.003.

Lin, Y.-C., Panchangam, S.C., Wu, C.-H., Hong, P.-K.A., Lin, C.-F., 2011. Effects of water washing on removing organic residues in bottom ashes of municipal solid waste incinerators. Chemosphere 82, 502–506. https://doi.org/10.1016/j.chemosphere.2010.11.010.

Loginova, E., Florea, M.V.A., Brouwers, H.J.H., 2017. Estimation of the environmental impact of MSWI bottom ash for reuse as a building material based on its composition. In: Proceedings of the 6th International Conference on Non-Traditional Cement and Concrete (NTCC). Brno, Czech Republic, 19–22 June, 2017, pp. 217–225.

Manders, J.L.C., 2009. The renewable energy contribution of waste to energy across Europe. In: Proceedings of the DAKOFA/ISWA Conference on Waste & Climate 2009. 3–4 December 2009, Copenhagen, Denmark.

Mangialardi, T., Paolini, A., Polettini, A., Sirini, P., 1999. Optimization of the solidification/stabilization process of MSW fly ash in cementitious matrices. J. Hazard. Mater. 70, 53–70. https://doi.org/10.1016/S0304-3894(99)00132-6.

McNeil, K., Thomas, H.K.K., 2013. Recycled concrete aggregates: a review. Int. J. Concr. Struct. Mater.

Mehta, P.K., Monteiro, P.J.M., 2014. Concrete: Microstructure, Properties, and Materials, fourth ed., McGraw-Hill Education, New York, Chicago, San Francisco, Athens, London, Madrid, Mexico City, Milan, New Delhi, Singapore, Sydney, Toronto.

Meima, J.A., Comans, R.N., 1999. The leaching of trace elements from municipal solid waste incinerator bottom ash at different stages of weathering. Appl. Geochem. 14, 159–171. https://doi.org/10.1016/S0883-2927(98)00047-X.

Meima, J.A., Comans, R.N.J., 1997. Geochemical modeling of weathering reactions in municipal solid waste incinerator bottom ash. Environ. Sci. Technol. 31, 1269–1276. https://doi.org/10.1021/es9603158.

Meima, J.A., van der Weijden, R.D., Eighmy, T.T., Comans, R.N., 2002. Carbonation processes in municipal solid waste incinerator bottom ash and their effect on the leaching of copper and molybdenum. Appl. Geochem. 17, 1503–1513. https://doi.org/10.1016/S0883-2927(02)00015-X.

Müller, U., Rübner, K., 2006a. The microstructure of concrete made with municipal waste incinerator bottom ash as an aggregate component. Cem. Concr. Res. 36, 1434–1443. https://doi.org/10.1016/j.cemconres.2006.03.023.

Müller, U., Rübner, K., 2006b. The microstructure of concrete made with municipal waste incinerator bottom ash as an aggregate component. Cem. Concr. Res. 36, 1434–1443. https://doi.org/10.1016/j.cemconres.2006.03.023.

Pacheco-Torgal, F., Jalali, S., 2010. Reusing ceramic wastes in concrete. Constr. Build. Mater. 24, 832–838. https://doi.org/10.1016/j.conbuildmat.2009.10.023.

Pacheco Torgal, F., 2013. Handbook of Recycled Concrete and Demolition Waste. Woodhead Publishing Ltd..

Pan, J.R., Huang, C., Kuo, J.-J., Lin, S.-H., 2008. Recycling MSWI bottom and fly ash as raw materials for Portland cement. Waste Manag. 28, 1113–1118. https://doi.org/10.1016/j.wasman.2007.04.009.

Pecqueur, G., Crignon, C., Quénée, B., 2001. Behaviour of cement-treated MSWI bottom ash. Waste Manag. 21, 229–233. https://doi.org/10.1016/S0956-053X(00)00094-5.

Qiao, X.C., Ng, B.R., Tyrer, M., Poon, C.S., Cheeseman, C.R., 2008a. Production of lightweight concrete using incinerator bottom ash. Constr. Build. Mater. 22, 473–480. https://doi.org/10.1016/j.conbuildmat.2006.11.013.

Qiao, X.C., Tyrer, M., Poon, C.S., Cheeseman, C.R., 2008b. Novel cementitious materials produced from incinerator bottom ash. Resour. Conserv. Recycl. 52, 496–510. https://doi.org/10.1016/j.resconrec.2007.06.003.

Quenee, B., Li, G., Siwak, J.M., Basuyau, V., 2000. Waste Materials in Construction Wascon 2000 – Proceedings of the International Conference on the Science and Engineering of Recycling for Environmental Protection, Harrogate, England 31 May, 1–2 June 2000, Waste Management Series, Waste Management Series. Elsevier. http://doi.org/10.1016/S0713-2743(00)80054-9.

Quina, M.J., Bordado, J.C., Quinta-Ferreira, R.M., 2008. Treatment and use of air pollution control residues from MSW incineration: an overview. Waste Manag. 28, 2097–2121. https://doi.org/10.1016/J.WASMAN.2007.08.030.

Saffarzadeh, A., Shimaoka, T., Motomura, Y., Watanabe, K., 2009a. Petrogenetic characteristics of molten slag from the pyrolysis/melting treatment of MSW. Waste Manag. 29, 1103–1113. https://doi.org/10.1016/j.wasman.2008.08.008.

Saffarzadeh, A., Shimaoka, T., Motomura, Y., Watanabe, K., 2009b. Characterization study of heavy metal-bearing phases in MSW slag. J. Hazard. Mater. 164, 829–834. https://doi.org/10.1016/j.jhazmat.2008.08.093.

Saffarzadeh, A., Shimaoka, T., Motomura, Y., Watanabe, K., 2006. Chemical and mineralogical evaluation of slag products derived from the pyrolysis/melting treatment of MSW. Waste Manag. 26, 1443–1452. https://doi.org/10.1016/J.WASMAN.2005.12.005.

Saikia, N., Cornelis, G., Mertens, G., Elsen, J., Van Balen, K., Van Gerven, T., Vandecasteele, C., 2008. Assessment of Pb-slag, MSWI bottom ash and boiler and fly ash for using as a fine aggregate in cement mortar. J. Hazard. Mater. 154, 766–777. https://doi.org/10.1016/j.jhazmat.2007.10.093.

Schollbach, K., Alam, Q., Caprai, V., Florea, M.V.A., Laan, S.R. van der, Hoek, C.J.G. van, Brouwers, H.J.H., 2016. Combined characterisation of mswi bottom ash. In: Proceedings of the Thirty-Eighth International Conference on Cement Microscopy. Lyon, France, 17-21 April 2016, pp. 74–82.

Seward, T.P., Vascott, T., 2006. High Temperature Glass Melt Property Database for Process Modeling. Wiley.

Shui, Z., Xuan, D., Wan, H., Cao, B., 2008. Rehydration reactivity of recycled mortar from concrete waste experienced to thermal treatment. Constr. Build. Mater. 22, 1723–1729. https://doi.org/10.1016/j.conbuildmat.2007.05.012.

Siddique, R., 2010. Use of municipal solid waste ash in concrete. Resour. Conserv. Recycl. 55, 83–91. https://doi.org/10.1016/j.resconrec.2010.10.003.

Silva, R.V., De Brito, J., Dhir, R.K., 2014. Properties and composition of recycled aggregates from construction and demolition waste suitable for concrete production. Constr. Build. Mater. 65. https://doi.org/10.1016/j.conbuildmat.2014.04.117.

Sorlini, S., Abbà, A., Collivignarelli, C., 2011. Recovery of MSWI and soil washing residues as concrete aggregates. Waste Manag. 31, 289–297. https://doi.org/10.1016/j.wasman.2010.04.019.

Spiesz, P., Rouvas, S., Brouwers, H.J.H., 2016. Utilization of waste glass in translucent and photocatalytic concrete. Constr. Build. Mater. 128, 436–448. https://doi.org/10.1016/J.CONBUILDMAT.2016.10.063.

Steketee, J.J., Duzijn, R.F., Born, J.G.P., 1997. Waste materials in construction - putting theory into practice. In: Proceedings of the International Conference on the Environment and Technical Implications of Construction with Alternative Materials, Studies in Environmental Science, Studies in Environmental Science. Elsevier. https://doi.org/10.1016/S0166-1116(97)80184-7.

Su, L., Guo, G., Shi, X., Zuo, M., Niu, D., Zhao, A., Zhao, Y., 2013. Copper leaching of MSWI bottom ash co-disposed with refuse: effect of short-term accelerated weathering. Waste Manag. 33, 1411–1417. https://doi.org/10.1016/j.wasman.2013.02.011.

Tang, P., Florea, M.V.A., Brouwers, H.J.H., 2016a. Recycling of waste materials as lightweigth aggregate by cold bonding pelletizing technique. In: Proceedings of the Thirty-Eighth International Conference on Cement Microscopy. Lyon, France, 17–21 April 2016, pp. 181–188.

Tang, P., Florea, M.V.A., Spiesz, P., Brouwers, H.J.H., 2016b. Application of thermally activated municipal solid waste incineration (MSWI) bottom ash fines as binder substitute. Cem. Concr. Compos. 70, 194–205. https://doi.org/10.1016/j.cemconcomp.2016.03.015.

Tang, P., Florea, M.V.A., Spiesz, P., Brouwers, H.J.H., 2015. Characteristics and application potential of municipal solid waste incineration (MSWI) bottom ashes from two waste-to-energy plants. Constr. Build. Mater. 83, 77–94. https://doi.org/10.1016/j.conbuildmat.2015.02.033.

van de Wouw, P.M.F., Florea, M.V.A., Brouwers, H.J.H., 2016. Processing disaster debris liberating aggregates for structural concrete. In: Schmidt, W., Msinjili, N. S. (Eds.), Proceedings of the 2nd International Conference on Advances in Cement and Concrete Technology in Africa (ACCTA). BAM Federal Institute for Materials Research and Testing, Berlin, Dar es Salaam, Tanzania, 27–29 January 2016, pp. 603–610.

Vegas, I., Ibañez, J.A., San José, J.T., Urzelai, A., 2008. Construction demolition wastes, Waelz slag and MSWI bottom ash: a comparative technical analysis as material for road construction. Waste Manag. 28, 565–574. https://doi.org/10.1016/j.wasman.2007.01.016.

Vries, W. de, Rem, P., Berkhout, P., 2009. ADR: a new method for dry classification. In: Proceedings of the ISWA International Conference, Lisbon, 12–15 October 2009.

Wei, Y., Mei, X., Shi, D., Liu, G., Li, L., Shimaoka, T., 2017. Separation and characterization of magnetic fractions from waste-to-energy bottom ash with an emphasis on the leachability of heavy metals. Environ. Sci. Pollut. Res. 24, 14970–14979. https://doi.org/10.1007/s11356-017-9145-8.

Wei, Y., Shimaoka, T., Saffarzadeh, A., Takahashi, F., 2011a. Mineralogical characterization of municipal solid waste incineration bottom ash with an emphasis on heavy metal-bearing phases. J. Hazard. Mater. 187, 534–543. https://doi.org/10.1016/J.JHAZMAT.2011.01.070.

Wei, Y., Shimaoka, T., Saffarzadeh, A., Takahashi, F., 2011b. Alteration of municipal solid waste incineration bottom ash focusing on the evolution of iron-rich constituents. Waste Manag. 31, 1992–2000. https://doi.org/10.1016/j.wasman.2011.04.021.

Wild, S., Gailius, A., Hansen, H., Pederson, L., Szwabowski, J., 1997. Pozzolanic properties of a variety of European clay bricks: Comparative study of pozzolanic, chemical and physical properties of clay bricks in four European countries for utilization of pulverized waste clay brick in production of mortar and concrete. Build. Res. Inf. 25, 170–175. https://doi.org/10.1080/096132197370435.

Wiles, C.C., 1996. Municipal solid waste combustion ash: State-of-the-knowledge. J. Hazard. Mater. 47, 325–344. https://doi.org/10.1016/0304-3894(95)00120-4.

Yang, R., Liao, W.-P., Wu, P.-H., 2012. Basic characteristics of leachate produced by various washing processes for MSWI ashes in Taiwan. J. Environ. Manage. 104, 67–76. https://doi.org/10.1016/j.jenvman.2012.03.008.

Yang, S., Saffarzadeh, A., Shimaoka, T., Kawano, T., 2014. Existence of Cl in municipal solid waste incineration bottom ash and dechlorination effect of thermal treatment. J. Hazard. Mater. 267, 214–220. https://doi.org/10.1016/j.jhazmat.2013.12.045.